

PAPER • OPEN ACCESS

## *In situ* off-axis electron holography of real-time dopant diffusion in GaAs nanowires

To cite this article: Ganapathi Prabhu Sai Balasubramanian *et al* 2022 *Nanotechnology* **33** 475705

View the [article online](#) for updates and enhancements.

### You may also like

- [Microfluidic system manufacturing by direct laser writing for the generation and characterization of microdroplets](#)  
Jonathan U Álvarez-Martínez, Orlando M Medina-Cázares, María E Soto-Alcaraz et al.
- [Warming in the Nordic Seas, North Atlantic storms and thinning Arctic sea ice](#)  
Vladimir A Alexeev, John E Walsh, Vladimir V Ivanov et al.
- [Invariance analysis, exact solutions and conservation laws of \(2+1\)-dimensional dispersive long wave equations](#)  
Kajal Sharma, Rajan Arora and Astha Chauhan



## Breath Biopsy<sup>®</sup> OMNI<sup>®</sup>

The most advanced, complete solution for global breath biomarker analysis

TRANSFORM YOUR RESEARCH WORKFLOW



Expert Study Design & Management



Robust Breath Collection



Reliable Sample Processing & Analysis






In-depth Data Analysis



Specialist Data Interpretation

# *In situ* off-axis electron holography of real-time dopant diffusion in GaAs nanowires

Ganapathi Prabhu Sai Balasubramanian<sup>1,\*</sup> , Elizaveta Lebedkina<sup>2</sup>,  
Nebile Isik Goktas<sup>3</sup>, Jakob Birkedal Wagner<sup>1</sup>, Ole Hansen<sup>1</sup>,  
Ray LaPierre<sup>3</sup> , Elizaveta Semenova<sup>2</sup>, Kristian Mølhave<sup>1</sup>,  
Marco Beleggia<sup>1</sup> and Elisabetta Maria Fiordaliso<sup>1,\*</sup> 

<sup>1</sup> DTU Nanolab, Technical University of Denmark, DK-2800 Kongens Lyngby, Denmark

<sup>2</sup> DTU Fotonik, Technical University of Denmark, DK-2800 Kongens Lyngby, Denmark

<sup>3</sup> Department of Engineering Physics, McMaster University, L8S 4L7 Hamilton, Ontario, Canada

E-mail: [gprabhus.balasubramanian@gmail.com](mailto:gprabhus.balasubramanian@gmail.com) and [emfi@dtu.dk](mailto:emfi@dtu.dk)

Received 26 January 2022, revised 29 June 2022

Accepted for publication 8 August 2022

Published 31 August 2022



CrossMark

## Abstract

Off-axis electron holography was used to reveal remote doping in GaAs nanowires occurring during *in situ* annealing in a transmission electron microscope. Dynamic changes to the electrostatic potential caused by carbon dopant diffusion upon annealing were measured across GaAs nanowires with radial p-p+ core-shell junctions. Electrostatic potential profiles were extracted from holographic phase maps and built-in potentials ( $V_{bi}$ ) and depletion layer widths (DLWs) were estimated as function of temperature over 300–873 K. Simulations in absence of remote doping predict a significant increase of  $V_{bi}$  and DLWs with temperature. In contrast, we measured experimentally a nearly constant  $V_{bi}$  and a weak increase of DLWs. Moreover, we observed the appearance of a depression in the potential profile of the core upon annealing. We attribute these deviations from the predicted behavior to carbon diffusion from the shell to the core through the nanowire sidewalls, i.e. to remote doping, becoming significant at 673 K. The DLW in the p and p+ regions are in the 10–30 nm range.

Supplementary material for this article is available [online](#)

Keywords: off-axis electron holography, carbon, GaAs, nanowire, COMSOL

(Some figures may appear in colour only in the online journal)

## 1. Introduction

The density of integrated electronic components continues to increase as the dimensions of individual devices shrink. Many semiconductor materials are synthesized in the form of nanowires (NWs) and employed as building blocks of high-performance nanoscale devices. NWs offer several advantages over traditional thin films. For example, they may

accommodate a large lattice mismatch, enabling new heterostructure material combinations and monolithic growth on inexpensive and widespread substrates such as Si [1, 2]. Semiconductor NWs are also employed in light emitting diodes, photovoltaics, photodetectors, solar cells, field-effect transistors and photonics [1, 3–8]. For these applications, it is essential to control the doping in the NWs, ideally with near-atomic resolution. Doping assessment at the nanoscale with techniques such as Raman spectroscopy [9], photoluminescence [10], Hall effect [11–13], time-resolved terahertz photoconductivity [14], capacitance–voltage measurements [15] and 4-point probe [16], is hampered by spatial resolution limitations. Other techniques targeting local chemical composition, such as secondary ion mass spectroscopy [17] and atom probe tomography [18] are also limited by their poor sensitivity

\* Authors to whom any correspondence should be addressed.



Original content from this work may be used under the terms of the [Creative Commons Attribution 4.0 licence](#). Any further distribution of this work must maintain attribution to the author(s) and the title of the work, journal citation and DOI.

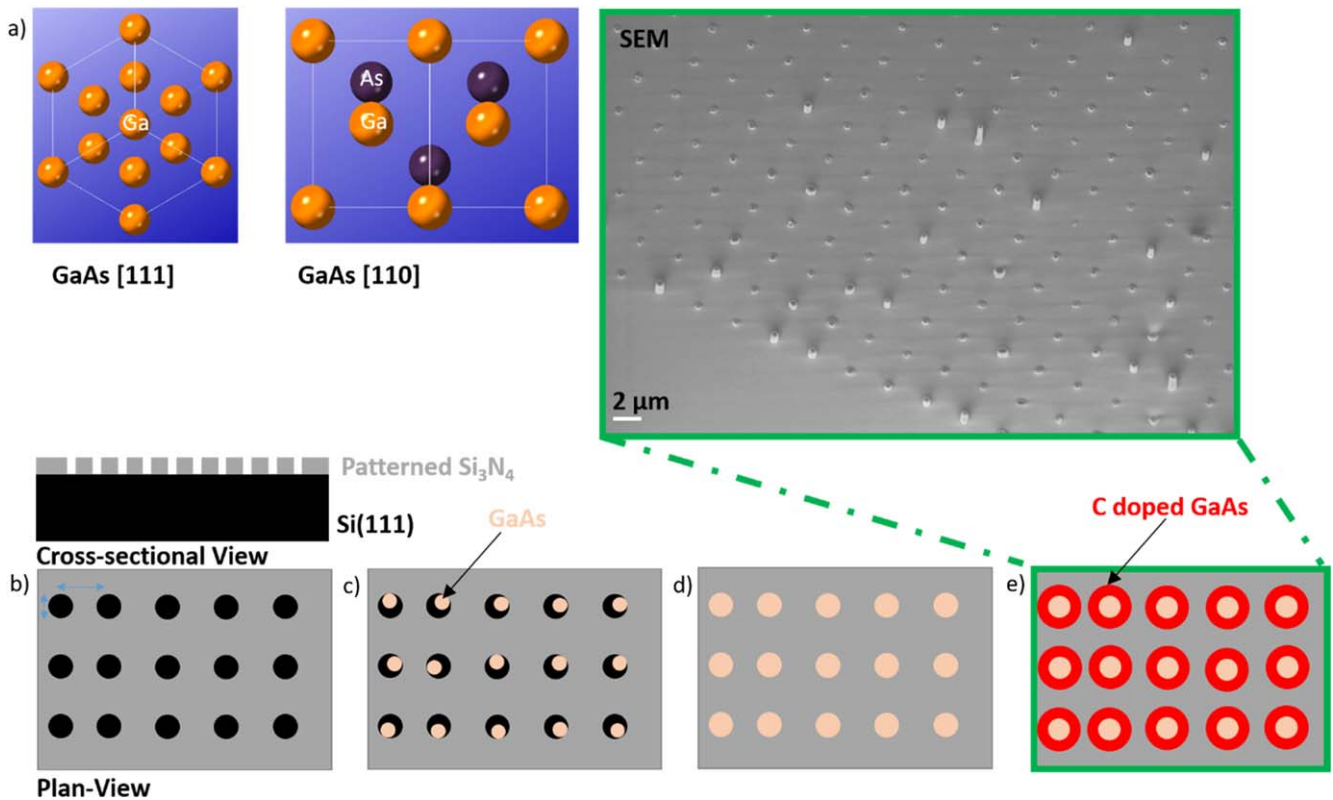


**Figure 1.** (a) Atomic arrangement in GaAs along [111] and [110] crystallographic directions. Lattice constant is 5.65325 Å. (b) Cross-sectional and plan views of the substrate with patterned dielectric layer for subsequent GaAs nuclei formation at the patterned sites. (c) Localization of the GaAs nuclei at the patterned sites during MOVPE growth of GaAs (core growth). (d) Radial growth of GaAs nanowire in (e) to yield an intentionally doped carbon doped shell. SEM image of the GaAs nanowires after the growth of the core and shell show a tilted view of the nanowires. In (b) the pitch and the diameter of the perforations are marked by horizontal and vertical arrows.

to active dopants. Off-axis electron holography (EH) [19–21] is an interferometric transmission electron microscopy (TEM) technique that measures a spatially resolved phase difference between the electrons passing through the specimen and those passing through vacuum. This phase difference encodes information on the potential variation across the sample relative to vacuum, which can then be retrieved. EH thus offers the unique combination of specific sensitivity to active dopants via the built-in potential they generate and nanoscale spatial resolution. EH has been employed for solid and liquid materials [21], has successfully profiled dopant distributions in p–n junctions [22–28], n-MOSFET/n-MOS [29, 30], i–n junctions [31], p–p+ junctions [32], and p–i–n radial structures [33, 34]. It has also been employed to monitor the state of dopant diffusion in a series of samples annealed *ex situ* [35]. In such case, direct comparison of holographic results is challenging, since different samples can be subjected to unequal artifacts introduced by the sample preparation techniques and by variation of TEM parameters at each measurement. In this work, EH was used to study *in situ* remote doping in GaAs NWs inside a TEM. We demonstrate the sensitivity of EH for detecting real-time changes to built-in potentials and depletion layer widths (DLWs) measured from electron holograms acquired as a function of temperature with resolutions of 0.1 V and 5 nm, respectively. The EH data reveal the maximal carbon dopant

concentration that GaAs NW can be doped with, and the carrier concentration in unintentionally doped GaAs NW core.

## 2. Methods

The radial core–shell GaAs NWs investigated in this work were grown selectively by metal organic vapor phase epitaxy (MOVPE) [36]. The core was nominally undoped (carrier concentration is  $1.79 \times 10^6 \text{ cm}^{-3}$  at 300 K) and the shell was highly carbon doped. The sample was epitaxially grown on pre-patterned Si(111) substrate by low pressure (80 mbar) metal organic vapour phase epitaxy system Turbodisc<sup>®</sup> Discovery 125 with H<sub>2</sub> as a carrier gas. The dielectric Si<sub>3</sub>N<sub>4</sub> mask deposited on Si surface consists of an array of 200 nm openings with pitch of 800 nm. The epitaxy process proceeded as follows: the core was grown using TMGa flow of 3 sccm, AsH<sub>3</sub> flow of 50 sccm, at a temperature of 1023 K for 1800 s. The shell was grown under TMGa flow of 20 sccm, AsH<sub>3</sub> flow of 50 sccm, dopant CBrCl<sub>3</sub> flow of 3 sccm, and growth time of 40 s at 898 K. The scheme successfully produced a radial growth as desired. Schematics of the growth process are shown in figure 1. The details on lamellae preparation can be found in the Supplementary Information.

The real-time measurements were performed in a FEI Titan Analytical 80–300ST TEM (ATEM) by *in situ* heating

of the cross-sectional samples using a Gatan double tilt tantalum heating holder, and acquiring electron holograms as a function of temperature, up to 873 K. Off-axis EH was performed using 120 keV electrons to remain below the knock-on damage threshold energy of 141.6 keV [37] with threshold displacement energy for GaAs of 10 eV [38]. For each temperature a series of object holograms and reference holograms in vacuum were obtained. The cross-sectional samples were tilted 2° from zone axis to minimize diffraction contrast. Similar diffraction conditions were used during *in situ* annealing and holography measurements. The sample temperature was raised with an estimated rate of ~20 K min<sup>-1</sup>, with dwell time at each target temperature of 30 min in average. The error bar for the quoted temperatures for the EH measurements is ~10 K.

As a first measurement, cross-sectional samples of GaAs NWs were annealed inside the TEM at temperatures up to 873 K. No deterioration of the NWs was observed during annealing. Previous works have shown that in the absence of arsenic flux the crystal structure remains intact when annealed up to ~950 K, but the GaAs NW morphology evolves [39, 40]. Thus, Ga and As evaporate stoichiometrically in the NWs up to 950 K [40]. The hydrogenated amorphous carbon (a-C:H) film surrounding the NWs, deposited during sample preparation protects the sidewalls preventing its evaporation. To assess dopant diffusion as a function of temperature, the expected potential profile and DLWs across the GaAs NWs were simulated with COMSOL Multiphysics software. Further details can be found in the Supplementary Information.

The measured holographic phase maps and the simulations were used to extract built-in potential ( $V_{bi}$ ) and DLWs as follows. In the absence of magnetic fields, the phase of the electron wave scattered by the sample relative to the phase of electrons passing through vacuum is given by [41]:

$$\varphi = C_E h_o (V_0 + V_f) \quad (1)$$

$$\Delta\varphi = C_E h_o (V_0 + V_{f,p+} - V_0 - V_{f,p}) = C_E h_o (V_{bi}), \quad (2)$$

where  $C_E$  is a constant that depends on the beam electron energy and is  $8.64 \times 10^6$  rad V<sup>-1</sup> m<sup>-1</sup> for 120 keV electrons [42],  $h_o$  is the thickness of the object,  $V_0$  is the mean inner potential of the solid, and  $V_f$  is the potential at the Fermi level in the individual p or p+ region prior to the junction formation.  $\Delta\varphi$  is the difference between  $\varphi$  for shell and core; since core and shell are made up of GaAs, the  $V_0$  is same for both. The built-in potential ( $V_{bi}$ ) is related to  $\Delta\varphi$  in equation (2). The crystalline thickness of the sample was estimated by convergent beam electron diffraction as  $250 \pm 5$  nm. Inactive amorphous layers at the top and bottom facets of the NW are expected to form as a result of FIB milling. Since at the end of the lamellae preparation we used a 2 keV Ga<sup>+</sup> ion beam for final polishing, the thickness of the amorphized layers is estimated to be ~1 nm based on an independent measurement on a Si sample [43]. Since these amorphized layers are significantly thinner than the sample, they were not considered in the measurement of  $V_{bi}$ .

The choice of NW thickness was based on optimizing the holography signal: as the sample thickness increases  $\Delta\varphi$

(equation (2)) increases, making it easier to detect phase changes across the junction; on the other hand, when the sample is too thick the fringe visibility  $\mu$  (equation (6)) drops due to increased inelastic scattering.

From 2D potential maps, line scans of potential were obtained. Then, sigmoidal logistic functions in equation (3) were used to fit the step function  $F(x)$  associated with the potential variation across the junction:

$$F(x) = A_2 + \frac{A_1 - A_2}{1 + \left(\frac{x}{x_0}\right)^p}, \quad (3)$$

where the fit parameters are  $A_1$ ,  $A_2$ ,  $x_0$  and  $p$ .  $V_{bi}$  is then given by:

$$V_{bi} = A_2 - A_1. \quad (4)$$

In addition to the statistical uncertainty of the fit, the thickness uncertainty will contribute to the error in  $V_{bi}$  via equation (2). However, in our measurements these are negligible when compared to the phase resolution given by:

$$\varphi_{min} = \frac{3}{\mu} \sqrt{\frac{2}{N}} \quad (5)$$

$$\mu = \frac{(I_{max} - I_{min})}{2 * N} * 100 \quad (6)$$

$$N = \frac{(I_{max} + I_{min})}{2}, \quad (7)$$

where  $\varphi_{min}$  is the minimum phase that can be detected between adjacent pixels in the acquired hologram [44].  $\mu$  and  $N$  are the fringe visibility and average counts, whereas  $I_{max}$  and  $I_{min}$  are the fringe's maximum and minimum counts. In our measurements on samples,  $I_{max}$ ,  $I_{min}$ ,  $\mu$  and  $\varphi_{min}$  are approximately 5500, 3000, 30% and 0.2 rad, respectively.

The error in  $V_{bi}$  is estimated as:

$$\frac{dV_{min}}{V_{bi}} = \frac{d\varphi_{min}}{\Delta\varphi} \quad (8)$$

$$dV_{min} = \frac{d\varphi_{min}}{\Delta\varphi/V_{bi}} = \frac{d\varphi_{min}}{C_E h_o}, \quad (9)$$

where  $dV_{min}$  is the error in  $V_{bi}$ , and  $V_{bi}$  and  $\Delta\varphi$  are the steps in potential and phase across the junction as in equation (2), respectively. With  $d\varphi_{min} \sim 0.2$  rad as above, we obtain  $dV_{min} \sim 0.1$  V.

### 3. Results

The DLW for the core and the shell at the junctions along each <110> direction were extracted from derivatives of the experimental potential profiles. Details are reported in the supplementary information (figure S1 (available online at [stacks.iop.org/NANO/33/475705/mmedia](https://stacks.iop.org/NANO/33/475705/mmedia))).

A sketch of the hexagonal cross-section of a p-p+ core-shell GaAs NW lying on a SiO<sub>2</sub>/Si substrate is shown in figure 2(a), whereas the reconstructed phase map from the hologram acquired at room temperature (RT) is shown in figure 2(b). Visual inspection of figure 2(b) clearly



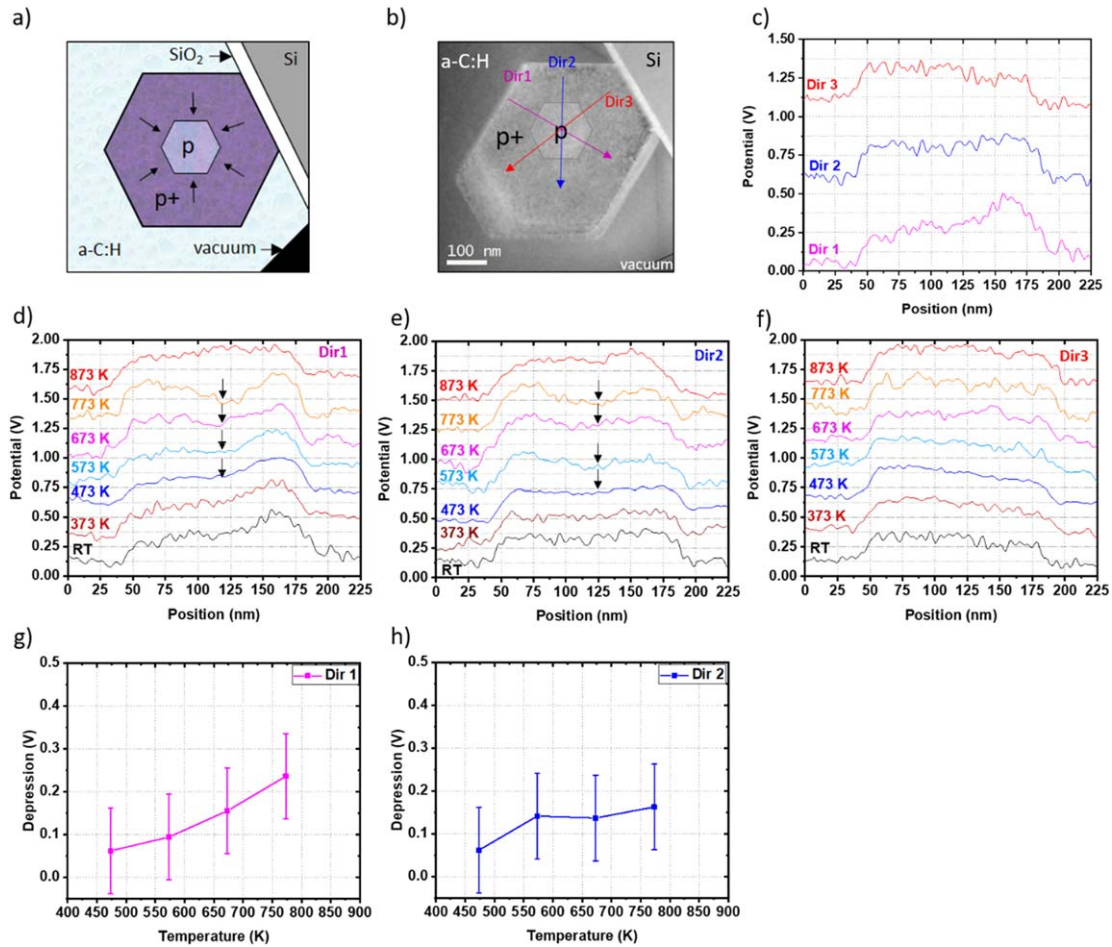


**Figure 2.** (a) Schematic cross-section of the NW. Arrows indicate diffusion direction of C from the shell into the core. (b) Reconstructed electrostatic potential map at RT. Arrows indicate the three  $\langle 110 \rangle$  directions, labelled Dir 1–3, which are normal to the facet edges (c) potential profiles at RT along Dir 1–3, centered with respect to the middle of the NW’s core. (d)–(f) Potential profiles from RT and 100 K to 873 K in 100 K steps for Dir 1–3, respectively. The arrows indicate the position of a depression within the core. The line scans are arbitrarily offset along the vertical direction. (g)–(h) Magnitude of the depression as a function of temperature for Dir 1 and 2.

distinguishes the p-core (bright contrast) from the p+ shell (dark contrast) and that the core is not at the center of the NW. The size of the core is 140 nm and shell is 95 and 126 nm thick along direction 1. In addition, the shape of the GaAs NWs is not a perfect hexagon, most likely caused by unequal local fluxes of Ga and As in equivalent crystallographic directions during growth of the NW. A similar effect was observed in [45], where it was shown that the III/V flux ratio as well as the individual III and V fluxes can affect the NW morphology. Additionally, growth temperature could also contribute to the morphology [45]. During the radial growth of our sample, the incorporation of carbon into the shell could also be affected by the neighbouring topography. Consistently, the RT line scans of the electrostatic potential extracted from the holographic phase map along the  $\langle 110 \rangle$  directions (labelled ‘Dir. 1–3’ in figure 2(c)) reveal a dopant concentration gradient across the NW.

The results of COMSOL simulations on  $V_{bi}$  for well-known cases of micron-scale pn and pp+ junctions are shown in figure S2 of the supplementary information. The almost-perfect match between simulations and theoretical expectations validates the simulations. To replicate our experimental

line scan profiles at RT in COMSOL, the hole density in the core was set to  $1.79 \times 10^6 \text{ cm}^{-3}$ – $1 \times 10^{17} \text{ cm}^{-3}$ , corresponding to a dopant range covering nominal intrinsic value for GaAs and significantly doped GaAs; the shell was kept at a hole concentration of  $1.5 \times 10^{20} \text{ cm}^{-3}$ . However, as shown in figure S3(a), in these cases the simulations deviated significantly for both potential line profiles (the potential profile in the core region had a curved top, which is not observed experimentally) and DLWs. Only by keeping the shell at a hole concentration of  $1.5 \times 10^{20} \text{ cm}^{-3}$  and increasing the hole density in the core to  $5 \times 10^{17} \text{ cm}^{-3}$  did we obtain simulated potential profiles wherein the fitted DLWs and the  $V_{bi}$  values became in reasonable agreement with the experimental values. Moreover, the potential curve in the core region features a linear top, as shown in figure S3(b), which best matches our experimental results. This suggests that the core is unintentionally doped rather than intrinsic, most likely by the methane produced as a by product during NW growth [46].

The electrostatic potential profiles along the direction 1–3 as a function of temperature are shown in figures 2(d)–(f). A change in shape of the electrostatic potential profile was

observed, showing a formation of a depression inside the core of the NW above 473 K (indicated by the arrow), which is more evident for directions 1 and 2. The magnitude of the depression increases with temperature. as shown in figures 2(g)–(h).

To gain insight into our experimental measurements, a 2D COMSOL model was created of a p-p+ core-shell GaAs NW with a linear dopant concentration gradient across it (figure S4) that best matches the RT data. The model keeps the dopant concentration gradient fixed over the temperature range to generate simulations in the absence of dopant diffusion. Circular NWs were simulated rather than the actual hexagonal NWs, because the  $V_{bi}$  and DLW depend on the size of the NW to a much greater extent than on its shape. By comparing the built-in potentials of a micron-scale and a nano-scale pp+ junction (figure S3(c)) we observe that size has a minor effect on . Therefore, by changing the shape of the object while preserving the size of the object cross-section, the effect on  $V_{bi}$  is expected to be negligible. Our simulations highlight a few important aspects. First, the diameter of the core (figure S5) affects the magnitudes of  $V_{bi}$  across the p-p+ junctions. Additionally, as the difference in dopant concentration between p and p + regions increases,  $V_{bi}$  increases (figure S6). Finally, our simulations show that  $V_{bi}$  increases with temperature (figures S4 and S7). By comparing figures S4 and S7, offsetting the core to one side of the shell has negligible effect on the  $V_{bi}$  and produces similar behavior of DLWs as a function of temperature. In the simulations shown in figure 3, the core was positioned at the geometric center of the shell since the trends are independent of the core offset.

Figure 3(a) labels the different junctions along directions 1–3 that were used for further analysis. The simulated  $V_{bi}$  and DLWs as a function of temperature are shown in figures 3(b) and (c), respectively. In our simulations where remote doping is absent,  $V_{bi}$  varied from 0.14 to 0.42 V for the junction at the interface ‘a’ and from 0.15 to 0.41 V for the junction at interface ‘b’, in the range of 300–873 K. The a and b junctions are marked in the simulation of figure S4 and are built to be equivalent to junctions 1a and 1b in figure 3(a). The DLWs in the core are 23–37 nm and 25–38 nm for the a and b junctions, respectively, in the temperature range investigated and they increase with temperature. The DLWs in the shell are 3–5 nm and ~5 nm for the a and b junctions, respectively, and do not significantly increase with temperature. The simulated  $V_{bi}$  as well as the DLW for the two junctions along the same direction are slightly different due to the dopant concentration gradient across the NW.

The experimental  $V_{bi}$  extracted from potential maps and estimated using equation (4) are shown in figures 3(d), (g) and (j) for the three  $\langle 110 \rangle$  directions. The values of  $V_{bi}$  averaged over junctions a and b and across the whole temperature range investigated are 0.3 V, 0.2 V and 0.2 V for directions 1–3, respectively, and they are constant with increasing temperature. The DLW for the 1a and 1b junctions are shown in figures 3(e)–(f). The DLWs for the core at the a and b junctions at RT are approximately 20 nm for all directions and they increase slightly with temperature. The DLWs for the

shells are essentially constant for all junctions in all directions as the temperature increases.

#### 4. Discussion

Contrary to the simulated behavior, a nearly constant  $V_{bi}$  was measured over 300–873 K. We first note that the electron beam was always on during the entire experimental run. This can stimulate doping by carbon contamination deposition over the irradiated area of the sample followed by enhanced penetration of carbon atoms into GaAs through momentum transfer or *in situ* annealing. Any electron beam assisted penetration of carbon atoms would naturally occur in the electron beam direction. Since the  $V_{bi}$  and DLW are measured on the sample in the directions perpendicular to the electron beam, any conceivable beam-induced doping must include carbon diffusion from shell to core. Further, during *in situ* annealing point defects can arise in the sample either produced by the electron beam or by the congruent evaporation of Ga and As species. These defects would be present all across the NW contribute as well to carbon diffusion through the sidewalls.

Next, the simulation data shown in figure 3(c) indicate that the DLW for the core, for example at 673 K, is significantly larger than that at RT. On the other hand, the DLW extracted from the experimental measurements for the core along any direction at RT and at 673 K do not show an increase that is comparable to that obtained in the simulations. The DLW increases with temperature and decreases with core doping. Therefore, a lack of significant variation of DLW with temperature can only exist when both these factors balance each other.

The DLW for the core is higher than that for the shell because of the difference in doping concentrations. The DLWs and the dopant concentrations in the shell remain essentially unchanged and this result agrees with the simulations. The radial dopant distribution across the NW is asymmetric prior to *in situ* annealing. However, the slight difference in the profile of  $V_{bi}$  with temperature for Dir 1–3 imply that carbon is incorporated in an asymmetric manner into the NW during *in situ* annealing.

Another indication that remote doping is taking place is the dynamic evolution of the depression in the electrostatic potential profile shown in figure 1, during *in situ* annealing. The depression in the electrostatic potential increases in magnitude with temperature and vanishes at 873 K. A possible explanation for the disappearance is out-diffusion of carbon to sufficient length at 873 K, causing flattening of the potential curve in the core region.

The C diffusivity in the bulk of GaAs NWs is different than that in bulk GaAs, which is described by [47]:

$$D = 5 \cdot 10^{-8} e^{-\frac{1.75}{kT}} \text{ cm}^2\text{s}^{-1} \quad (10)$$

with  $kT$  expressed in eV. From the diffusivity, the diffusion length can be estimated as  $L = 2\sqrt{Dt}$ , where  $t$  is time. Equation (10) predicts a length of 0.03 nm at 673 K for a

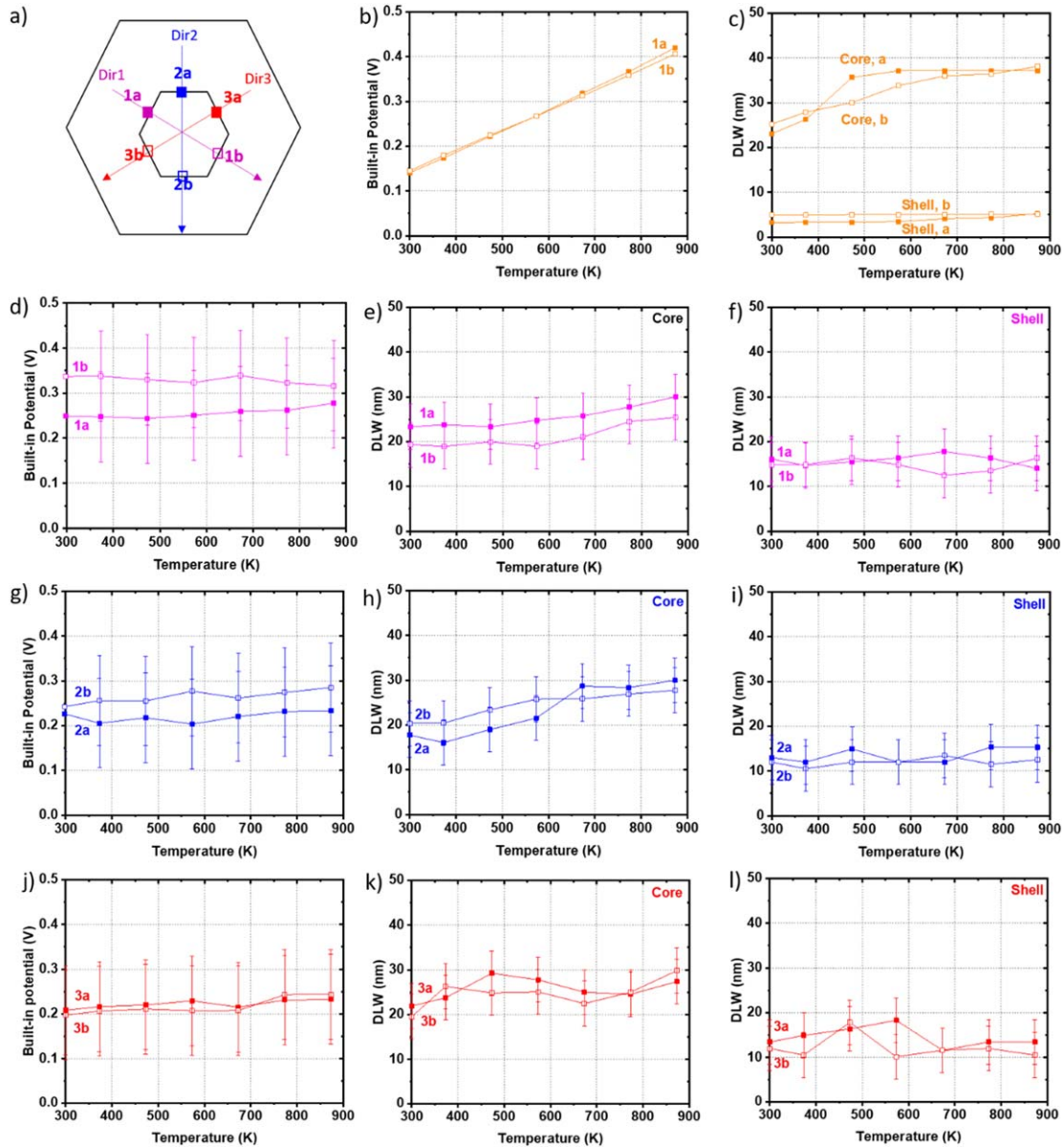


**Figure 3.** (a) Sketch of the cross-sectional NW with  $\langle 110 \rangle$  directions labelled 1–3, normal to the facet edges. (b)–(c) Simulated  $V_{bi}$  and DLW as a function of temperature and in the absence of remote doping. (d)–(l) Experimental values of  $V_{bi}$  and DLW for core and shell along  $\langle 110 \rangle$  directions: (d)–(f), direction 1; (g)–(i), direction 2, and; (j)–(l) direction 3.

$\sim 10$  min time scale, which is negligible. We thus infer that C diffusion in GaAs NWs could be much larger than in bulk GaAs. First, this is consistent with two orders of magnitude diffusion enhancement in Si NWs compared to bulk Si [18]. Second, NWs have twins [48, 49] and intrinsic defects [50] from the growth, and during any subsequent annealing additional defects such as column III antisites, column III interstitials and As vacancies [51] are expected. These defects might cause enhanced dopant diffusion. Third, we expect that as the incongruent sublimation temperature increases in GaAs NWs, the diffusivity increases (figure S8).

The enhanced diffusion of C in GaAs NW makes possible remote doping through the side facets defining the edges of the core. Doping through the side facets is consistent with what has been reported for Be dopants [52] and Si dopants [53] in GaAs. However, unlike the Be dopants which

preferentially incorporates along 3-fold symmetric truncated facets of GaAs NWs [33], C doped regions in our remote doping experiment do not show strong segregation within the core or shell.

## 5. Conclusion

In conclusion, we successfully fabricated GaAs NWs with radial p-p+ junctions and used off-axis EH to observe their remote doping initiated by *in situ* annealing inside a transmission electron microscope. COMSOL simulations show that for a fixed diameter of the shell, the  $V_{bi}$  increases with core diameter. Carbon doping of GaAs during growth in a MOVPE process can lead to a p-p+ core-shell radial structure in NWs with a highly doped shell i.e.  $\sim 1.5 \times 10^{20}$  dopant  $\text{cm}^{-3}$  and a



core that is unintentionally doped to  $\sim 5 \times 10^{17}$  dopant  $\text{cm}^{-3}$ . Further, we quantify remote doping in these NWs through measurements of  $V_{bi}$  and DLW. The combination of (i) the progressive formation of a depression in the potential profile inside the core with increasing temperature, which is significant at 673 K (ii) the weak variation of  $V_{bi}$  with temperature, along any direction, and (iii) the variations of simulated DLWs with temperature, strongly suggest that C diffusion in GaAs NWs is significantly larger than that in bulk GaAs above 673 K. Carbon is incorporated effectively through the {110} bounding facets of the NW core and the slight difference in the  $V_{bi}$  and DLW as function of temperature for each equivalent  $\langle 110 \rangle$  direction indicates asymmetric incorporation of C during *in situ* annealing. Defects produced by the electron beam irradiation and those resulting from congruent evaporation of Ga and As could lead to enhanced diffusion of carbon in the NWs.

## Acknowledgments

This work was supported by a research Grant (00022965) from VILLUM FONDEN.


## Data availability statement

All data that support the findings of this study are included within the article (and any supplementary files).

## Supplementary information

Details on the nanowire growth and lamellae preparation, details of EH measurements, material properties used in simulation, procedure for extracting depletion layer widths, simulations for micron-scale pn and pp+ junctions in GaAs, simulations of nanoscale pp+ junctions in GaAs with no dopant concentration gradient across the structure, simulations for the core-shell structured sample, C diffusion lengths in GaAs bulk and NWs, and references.

## ORCID iDs

Ganapathi Prabhu Sai Balasubramanian  <https://orcid.org/0000-0002-3959-5764>

Ray LaPierre  <https://orcid.org/0000-0003-4598-8940>

Elisabetta Maria Fiordaliso  <https://orcid.org/0000-0002-1221-2604>

## References

- [1] Zhang Y, Wu J, Aagesen M and Liu H 2015 III–V nanowires and nanowire optoelectronic devices *J. Phys. Appl. Phys.*, **48** 463001
- [2] Kavanagh K L 2010 Misfit dislocations in nanowire heterostructures *Semicond. Sci. Technol.* **25** 024006
- [3] Krogstrup P, Jørgensen H I, Heiss M, Demichel O, Holm J V, Aagesen M, Nygard J and I Morral A F 2013 Single-nanowire solar cells beyond the shockley–queisser limit *Nat. Photon.* **7** 4
- [4] Li Y, Qian F, Xiang J and Lieber C M 2006 Nanowire electronic and optoelectronic devices *Mater. Today* **9** 18–27
- [5] Kim H-M, Cho Y-H, Lee H, Kim S I, Ryu S R, Kim D Y, Kang T W and Chung K S 2004 High-brightness light emitting diodes using dislocation-free indium gallium nitride/gallium nitride multiquantum-well nanorod arrays *Nano Lett.* **4** 1059–62
- [6] Joyce H J *et al* 2011 III–V semiconductor nanowires for optoelectronic device applications *Prog. Quantum Electron.* **35** 23–75
- [7] Bryllert T, Wernersson L-E, Löwgren T and Samuelson L 2006 Vertical wrap-gated nanowire transistors *Nanotechnology* **17** S227–30
- [8] Czaban J A, Thompson D A and LaPierre R R 2009 GaAs core-shell nanowires for photovoltaic applications *Nano Lett.* **9** 148–54
- [9] Suomalainen S, Hakkarainen T V, Salminen T, Koskinen R, Honkanen M, Luna E and Guina M 2015 Te-doping of self-catalyzed GaAs nanowires *Appl. Phys. Lett.* **107** 012101
- [10] Arab S, Yao M, Zhou C, Daniel Dapkus P and Cronin S B 2016 Doping concentration dependence of the photoluminescence spectra of n-type GaAs nanowires *Appl. Phys. Lett.* **108** 182106
- [11] Blömers C, Grap T, Lepsa M I, Moers J, Trelenkamp S, Grützmacher D, Lüth H and Schäpers T 2012 Hall effect measurements on InAs nanowires *Appl. Phys. Lett.* **101** 152106
- [12] Heurlin M, Hultin O, Storm K, Lindgren D, Borgström M T and Samuelson L 2014 Synthesis of doped InP core-shell nanowires evaluated using hall effect measurements *Nano Lett.* **14** 749–53
- [13] Storm K, Halvardsson F, Heurlin M, Lindgren D, Gustafsson A, Wu P M, Monemar B and Samuelson L 2012 Spatially resolved Hall effect measurement in a single semiconductor nanowire *Nat. Nanotechnol.* **7** 718–22
- [14] Boland J L, Casadei A, Tütüncioğlu G, Matteini F, Davies C L, Jabeen F, Joyce H J, Herz L M, I Morral A F and Johnston M B 2016 Increased photoconductivity lifetime in GaAs nanowires by controlled n-type and p-type doping *ACS Nano* **10** 4219–27
- [15] Garnett E C, Tseng Y-C, Khanal D R, Wu J, Bokor J and Yang P 2009 Dopant profiling and surface analysis of silicon nanowires using capacitance–voltage measurements *Nat. Nanotechnol.* **4** 311–4
- [16] Wirths S *et al* 2011 Effect of Si-doping on InAs nanowire transport and morphology *J. Appl. Phys.* **110** 053709
- [17] Chia A C E, Dhindsa N, Boulanger J P, Wood B A, Saini S S and LaPierre R R 2015 Nanowire dopant measurement using secondary ion mass spectrometry *J. Appl. Phys.* **118** 114306
- [18] Chen W, Dubrovskii V G, Liu X, Xu T, Lardé R, Nys J P, Grandidier B, Stiévenard D, Patriarche G and Pareige P 2012 Boron distribution in the core of Si nanowire grown by chemical vapor deposition *J. Appl. Phys.* **111** 094909
- [19] Electron Holography Methods 1996 Handbook of Microscopy Set (John Wiley & Sons, Ltd.) 515–36
- [20] Lehmann M and Lichte H 2002 Tutorial on Off-axis electron holography *Microsc. Microanal.* **8** 447–66
- [21] Hyllested J A, Balasubramanian G P S, Fiordaliso E M, Yesibolati M, Møllhave K and Beleggia M 2020 Electron holography in gaseous and liquid environment *Microsc. Microanal.* **26** 2488–9



- [22] Yazdi S, Kasama T, Beleggia M, Yekt M S, McComb D W, Twitchett-Harrison A C and Dunin-Borkowski R E 2015 'Towards quantitative electrostatic potential mapping of working semiconductor devices using off-axis electron holography *Ultramicroscopy* **152** 10–20
- [23] Twitchett A C, Dunin-Borkowski R E, Hallifax R J, Broom R F and Midgley P A 2004 'Off-axis electron holography of electrostatic potentials in unbiased and reverse biased focused ion beam milled semiconductor devices *J. Microsc.* **214** 287–96
- [24] Cooper D, Ailliot C, Barnes J-P, Hartmann J-M, Salles P, Benassayag G and Dunin-Borkowski R E 2010 Dopant profiling of focused ion beam milled semiconductors using off-axis electron holography, reducing artifacts, extending detection limits and reducing the effects of gallium implantation *Ultramicroscopy* **110** 383–9
- [25] Darbandi A, McNeil J C, Akhtari-Zavareh A, Watkins S P and Kavanagh K L 2016 Direct measurement of the electrical abruptness of a nanowire p–n junction *Nano Lett.* **16** 3982–8
- [26] Sasaki H, Yamamoto K and Hirayama T 2006 Mapping of dopant concentration in a GaAs semiconductor by off-axis phase-shifting electron holography *Appl. Phys. Lett.* **89** 244101
- [27] Gan Z, Perea D E, Yoo J, Tom Picraux S, Smith D J and McCartney M R 2013 Mapping electrostatic profiles across axial p-n junctions in Si nanowires using off-axis electron holography *Appl. Phys. Lett.* **103**153108
- [28] Hakkarainen T *et al* 2019 Te incorporation and activation as n-type dopant in self-catalyzed GaAs nanowires *Phys. Rev. Mater.* **3** 086001
- [29] Wolf D, Lubk A, Prete P, Lovergine N and Lichte H 2016 3D mapping of nanoscale electric potentials in semiconductor structures using electron-holographic tomography *J. Phys. Appl. Phys.* **49** 364004
- [30] Cooper D, Béch e A, Servanton G, Pantel R, Morin P and Rouviere J-L 2011 Nano-field mapping for the semiconductor industry *J. Phys. Conf. Ser.* **326** 012054
- [31] Goktas N I, Fiordaliso E M and LaPierre R R 2018 Doping assessment in GaAs nanowires *Nanotechnology* **29** 234001
- [32] Amichi L, Mouton I, Di Russo E, Boureau V, Barbier F, Dussaigne A, Grenier A, Jouneau P-H, Bougerol C and Cooper D 2020 Three-dimensional measurement of Mg dopant distribution and electrical activity in GaN by correlative atom probe tomography and off-axis electron holography *J. Appl. Phys.* **127** 065702
- [33] Dastjerdi M H T, Fiordaliso E M, Leshchenko E D, Akhtari-Zavareh A, Kasama T, Aagesen M, Dubrovskii V G and LaPierre R R 2017 Three-fold symmetric doping mechanism in GaAs nanowires *Nano Lett.* **17** 5875–82
- [34] Boulanger J P, Chia A C E, Wood B, Yazdi S, Kasama T, Aagesen M and LaPierre R R 2016 Characterization of a Ga-assisted GaAs nanowire array solar cell on si substrate *IEEE J. Photovolt.* **6** 661–7
- [35] Rau W-D and Orchowski A 2004 Mapping of process-induced dopant redistributions by electron holography *Microsc. Microanal.* **10** 462–9
- [36] Yao M, Sheng C, Ge M, Chi C-Y, Cong S, Nakano A, Dapkus P D and Zhou C 2016 Facile five-step heteroepitaxial growth of GaAs nanowires on silicon substrates and the twin formation mechanism *ACS Nano* **10** 2424–35
- [37] Williams D B and Carter C B 2009 Inelastic scattering and beam damage *Transmission Electron Microscopy: A Textbook for Materials Science* ed D B Williams and C B Carter (Boston, MA: Springer US) pp 53–71
- [38] Hausmann H, Pillukat A and Ehrhart P 1996 Point defects and their reactions in electron-irradiated GaAs investigated by optical absorption spectroscopy *Phys. Rev. B* **54** 8527–39
- [39] Ilkiv I, Kirilenko D, Kotlyar K and Bouravlev A 2019 Thermal decomposition of GaAs nanowires *Nanotechnology* **31** 055701
- [40] Loitsch B *et al* 2015 Tunable quantum confinement in ultrathin, optically active semiconductor nanowires via reverse-reaction growth *Adv. Mater.* **27** 2195–202
- [41] Rau W D, Schwander P, Baumann F H, H oppner W and Ourmazd A 1999 Two-dimensional mapping of the electrostatic potential in transistors by electron holography *Phys. Rev. Lett.* **82** 2614–7
- [42] Kasama T, Dunin-Borkowski R E and Beleggia M 2011 Electron holography of magnetic materials *Holography - Different Fields of Application* ed F A M Ram rez (InTech) pp 53–80 (<http://intechopen.com/books/show/title/holography-different-fields-of-application>)
- [43] Giannuzzi L A, Geurts R and Ringnalda J 2005 2 keV Ga + FIB milling for reducing amorphous damage in silicon *Microsc. Microanal.* **11** 828–9
- [44] Lichte H 2008 Performance limits of electron holography *Ultramicroscopy* **108** 256–62
- [45] Soci C, Bao X-Y, Aplin D P R and Wang D 2008 'A Systematic study on the growth of GaAs nanowires by metal–organic chemical vapor deposition *Nano Lett.* **8** 4275–82
- [46] Lin A L, Dao V and Donaghey L F Kinetics of the chemical vapor deposition of GaAs from Ga(CH<sub>3</sub>)<sub>3</sub> and AsH<sub>3</sub> *Presented at the Proc. of the 6th Int. Conf. on Chemical Vapor Deposition (Atlanta)* GA, Aug. 1977. Accessed: Aug. 22, 2021 [Online]. Available: <https://escholarship.org/uc/item/6n58z8jh>
- [47] Schubert E F 1993 *Doping in III-V Semiconductors*. Cambridge (Cambridge: Cambridge University Press) Section 8.4.4 p 329
- [48] Yoshida H, Ikejiri K, Sato T, Hara S, Hiruma K, Motohisa J and Fukui T 2009 Analysis of twin defects in GaAs nanowires and tetrahedra and their correlation to GaAs(111)B surface reconstructions in selective-area metal organic vapour-phase epitaxy *J. Cryst. Growth* **312** 52–7
- [49] Burgess T, Breuer S, Caroff P, Wong-Leung J, Gao Q, Tan H H and Jagadish C 2013 'Twinning superlattice formation in GaAs nanowires *ACS Nano* **7** 8105–14
- [50] Liu L, Diao Y and Xia S 2020 Intrinsic point defects in pristine and Zn-doped GaAs nanowire surfaces: a first-principles investigation *Appl. Surf. Sci.* **514** 145906
- [51] Pavesi L 1992 Role of point defects in the silicon diffusion in GaAs and Al<sub>0.3</sub>Ga<sub>0.7</sub>As and in the related superlattice disordering *J. Appl. Phys.* **71** 2225–37
- [52] Casadei A, Krogstrup P, Heiss M, R ohr J A, Colombo C, Ruelle T, Upadhyay S, S orensen C B, Nyg ard J and I Morral A F 2013 Doping incorporation paths in catalyst-free Be-doped GaAs nanowires *Appl. Phys. Lett.* **102** 013117
- [53] Dufouleur J, Colombo C, Garma T, Ketterer B, Uccelli E, Nicotra M and Morral A F I 2010 P-doping mechanisms in catalyst-free gallium arsenide nanowires *Nano Lett.* **10** 1734–40